Adiabatic passage of ²⁰⁵TlF with microwaves in a cryogenic beam

Olivier Grasdijk,^{1,*} Jakob Kastelic,² Jianhui Li,³ Oskari Timgren,² Konrad Wenz,³ Yuanhang Yang,⁴ Perry Zhou,³ David Kawall,⁵ Tanya Zelevinsky,³ and David DeMille^{6,†} (CeNTREX Collaboration)

¹Physics Division, Argonne National Laboratory, Argonne, Illinois 60439, USA
²Department of Physics, Yale University, New Haven, Connecticut 06511, USA
³Department of Physics, Columbia University, New York, New York 10027, USA
⁴Department of Physics, University of Chicago, Chicago, Illinois 60637, USA
⁵Department of Physics, University of Massachusetts Amherst, Amherst, Massachusetts 01003, USA
⁶Department of Physics and Astronomy, Johns Hopkins University, Baltimore, Maryland 21218, USA
(Dated: November 21, 2025)

We present a hyperfine-resolved state preparation scheme for thallium fluoride (TIF) molecules based on microwave-driven adiabatic passage (AP) in a spatially varying electric field. This method enables efficient and robust population transfer between selected $|J,m_J=0\rangle$ hyperfine sublevels of the $X^{-1}\Sigma_0^+$ ground state in a cryogenic molecular beam, a key requirement for the CeNTREX search for nuclear time-reversal symmetry violation. Two sequential stages of AP are implemented. The first transfers population from J=0 to J=1 at a local field of 173 V/cm, and the second transfers from J=1 to J=2 at 110 V/cm. Transfer efficiencies are quantified through laser-induced fluorescence, and accounting for residual population in excited rotational levels after a prior stage of rotational cooling. We achieve state transfer efficiencies of 0.92(6) and 1.05(5) for the first and second states of AP, respectively. This corresponds to a total efficiency of 0.97(8) for population transfer from J=0 to J=2. These results demonstrate robust and high-fidelity preparation of specific rotational/hyperfine states in TIF.

I. INTRODUCTION

CeNTREX (the Cold Molecule Nuclear Time-Reversal Experiment) seeks to achieve a significant improvement in sensitivity beyond the current best upper limits on the strength of certain hadronic time-reversal (T)-violating fundamental interactions, such as the proton electric dipole moment and the CP-violating quantum chromodynamics parameter, $\bar{\theta}_{\rm QCD}$. The overall CeNTREX approach and measurement strategy are discussed in [1]. By conducting magnetic resonance measurements on the ²⁰⁵Tl nucleus within an electrically polarized thallium monofluoride (TlF) molecule, CeNTREX aims to determine the Schiff moment of ²⁰⁵Tl. The strongly polarized electron shells in TIF couple strongly to the Schiff moment, resulting in magnetic resonance frequency shifts that are orders of magnitude larger than those achievable in atomic experiments, for the same size of Schiff moment [2].

The CeNTREX protocol requires preparing TlF molecules in a variety of different rotational and hyperfine states at different stages of the experiment: efficient rotational cooling [3], molecular beam collimation via electrostatic lenses [1], implementation of the Schiff-moment measurement sequence [4], and nuclear-spin readout via optical cycling [1]. CeNTREX plans to implement trans-

fer between these states using microwave-driven adiabatic passage (AP).

Adiabatic passage is a robust method for coherently transferring population between quantum states [5–7]. Unlike π -pulses, which require precise control of intensity and timing, AP achieves near-unity transfer efficiency whenever the adiabatic condition is satisfied, making it ideal for molecular beam experiments with spatial and velocity inhomogeneities [8]. Here we demonstrate a state-transfer scheme for CeNTREX that employs microwave AP in spatially varying electric fields to transfer population from specific hyperfine sublevels of $|J=0\rangle$ to other specific hyperfine states in the $|J=2\rangle$ manifold of states, all within the TIF ground electronic state.

Adiabatic passage is closely related to the Landau–Zener mechanism [9], in which two states, $|\downarrow\rangle$ and $|\uparrow\rangle$, are coupled with strength $\Omega/2$ while their energy separation Δ is swept through zero. The Hamiltonian for such a two-level system is

$$H = \frac{1}{2} \begin{pmatrix} -\Delta(t) & \Omega \\ \Omega & \Delta(t) \end{pmatrix} \tag{1}$$

with $\Delta(t) = kt$ and constant coupling Ω . A similar form describes a driven two-level system under the rotating wave approximation.

The time evolution of the system (Fig. 1) depends on the rate at which the detuning $\Delta(t)$ varies relative to the coupling strength Ω . For the Landau–Zener model, the final state can be solved analytically [9], making it a useful benchmark for more general situations. Different

^{*} jgrasdijk@argonne.gov

[†] david.demille@jhu.edu; Also at Physics Division, Argonne National Laboratory, Argonne, Illinois 60439, USA and Department of Physics, University of Chicago, Chicago, Illinois 60637, USA

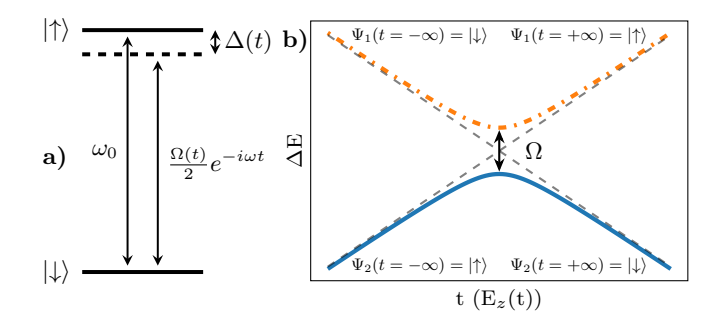


FIG. 1. a) A two-level system with energy splitting ω_0 , where the states are coupled by an oscillating field with frequency $\omega(t)$ and a Rabi rate $\Omega(t)/2$. In the rotating frame, the Hamiltonian simplifies to the form shown in Eqn. (1), incorporating time-dependent Rabi rate $\Omega(t)$ and non-linear detuning $\Delta(t)$. Under the rotating wave approximation, this Hamiltonian also describes microwave-driven rotational transitions in TIF. b) Eigenenergies of the Landau-Zener system as the detuning $\Delta(t)$, here due to a time-varying $E_z(t)$, evolves from $\Delta \to -\infty$ $(t \to -\infty)$ to $\Delta \to +\infty$ $(t \to +\infty)$. The ground state transitions from $\Psi(t \to -\infty) = |\uparrow\rangle$ to $\Psi(t \to +\infty) = |\downarrow\rangle$. Under adiabatic conditions $(\frac{d\Delta}{dt} \ll \Omega^2)$, the system follows the instantaneous eigenstates, remaining in the ground state if initially prepared there.

regimes are characterized by the rapidity parameter

$$\Gamma = \frac{\frac{d\Delta}{dt}}{\Omega^2}.$$
 (2)

In the adiabatic limit ($\Gamma \ll 1$), the state vector follows the instantaneous eigenstates, leading to complete population inversion between $|\downarrow\rangle$ and $|\uparrow\rangle$. In the sudden limit ($\Gamma \gg 1$), the system remains in its initial state $|\downarrow\rangle$. For intermediate values ($\Gamma \sim 1$), the final state is a coherent superposition of $|\downarrow\rangle$ and $|\uparrow\rangle$.

Adiabatic passage corresponds to the adiabatic regime, where $\Gamma = \frac{d\Delta}{dt}/\Omega^2 \ll 1$. Here, Ω is typically set by the strength of an oscillating drive field (e.g., a microwave), and Δ is the detuning between the drive frequency and the transition (e.g. due to an electric field). After transforming to the rotating frame and applying the rotating wave approximation, the dynamics reduce to the Hamiltonian in Eqn. (1).

A major advantage of adiabatic passage over the conventional π -pulse method is its robustness [8]. Once the adiabatic condition ($\Gamma \ll 1$) is satisfied, population inversion occurs with nearly unit efficiency. This insensitivity to variations in drive strength and interaction time is particularly valuable in a molecular beam, where molecules experience different microwave intensities and transit times. Provided the coupling is sufficiently strong, AP ensures nearly uniform transfer efficiency across the ensemble.

A beam of cold TIF molecules is produced using a cryogenic buffer-gas source [1, 10], which provides high flux, low forward velocity, narrow velocity spread, and low rotational temperature. For Centre X, neon cooled to

19 K serves as the buffer gas, offering higher repetition rates and more stable flux for heavy species such as TlF compared to helium [11]. After further cooling in the free expansion of the neon flow, the TlF beam reaches a rotational temperature of 6.3(2) K [1]. At this temperature only $\sim 5\%$ of the molecules occupy the lowest rotational state J=0, and just one quarter of that fraction is in the absolute ground state $|J=0,F=0\rangle$. To increase this population, rotational cooling is applied: a combination of microwave and laser fields transfers population from all hyperfine sublevels of the three lowest excited rotational levels (J=1,2,3) into the J=0 hyperfine manifold, enhancing the $|J=0,F=0\rangle$ population by a factor of ≈ 20 [3].

To collimate the diverging molecular beam, an electrostatic quadrupole lens (EQL) will be employed. This requires molecules to occupy a state with a positive quadratic Stark shift, which is realized in $|J=2,m_J=0\rangle$. Population transfer from $|J=0,F=0\rangle$ to particular hyperfine sublevels of $|J=2,m_J=0\rangle$ can be implemented via two sequential microwave-driven adiabatic passages. The necessary time-varying detuning for AP is provided by the second-order DC Stark effect: as molecules traverse a spatially varying DC electric field, the resonance frequencies of the rotational transitions shift accordingly.

In CeNTREX, the goal is to transfer population between selected hyperfine levels of different rotational states. Microwave electric fields provide the coupling, while spatially varying DC electric fields produce the required detuning. By engineering both the magnitude and gradient of the DC field, and simultaneously applying near-resonant microwaves, robust adiabatic passage can be achieved.

The simple Landau–Zener model is insufficient here because of the non-linear time dependence of the detuning, the spatially varying coupling strength (i.e., microwave intensity), and the presence of multiple, near-resonantly coupled hyperfine/rotational levels. Hence, we perform numerical simulations of the full TlF Hamiltonian, including levels up to J=4. These simulations confirmed that efficient transfer between selected hyperfine/rotational states can be achieved when the adiabatic condition $\Gamma \ll 1$ is satisfied [6].

It is important to minimize stray microwave fields because any residual field outside the intended AP region can coherently transfer population back toward the initial state and reduce the net transfer. Additionally nonlinear polarization or small transverse components in the microwave field couple hyperfine and magnetic sublevels that are not included in the designed transfer chain.

A. TlF in varying electric fields

The experiment described here performs AP in a DC electric field of $\sim 100\,\mathrm{V/cm}$, with state detection at zero field. The eigenstates of TlF differ significantly

TABLE I. Constants for rotational, hyperfine, and Stark interactions in the effective TlF ground-state Hamiltonian [Eq. (4)].

between these regimes due to the combined rotational and hyperfine structure of the $X^{1}\Sigma_{0}^{+}$, v=0 ground state [1]. Rotational structure arises from the diatomic molecule's center-of-mass rotation, while both 205 Tl and 19 F nuclei have spin 1 /2, producing hyperfine splittings from spin–rotation and spin–spin couplings. The effective Hamiltonian, including rotational, spin–rotation, spin–spin, and Stark interactions, is given by

$$\mathcal{H}_{TlF} = \mathcal{H}_{rot} + \mathcal{H}_{sr} + \mathcal{H}_{ss} + \mathcal{H}_{S}, \tag{3}$$

with

$$\mathcal{H}_{\text{rot}} = B\mathbf{J}^{2},$$

$$\mathcal{H}_{\text{sr}} = c_{1}(\mathbf{I}_{1} \cdot \mathbf{J}) + c_{2}(\mathbf{I}_{2} \cdot \mathbf{J}),$$

$$\mathcal{H}_{\text{ss}} = c_{3}T^{2}(\mathbf{C}) \cdot T^{2}(\mathbf{I}_{1}, \mathbf{I}_{2}) + c_{4}(\mathbf{I}_{1} \cdot \mathbf{I}_{2}),$$

$$\mathcal{H}_{S} = -\mu_{e} \cdot \boldsymbol{\mathcal{E}},$$

$$(4)$$

where constants are listed in Table I. In the ground state, TlF lacks opposite-parity near-degeneracies, so the Stark interaction appears only at second order.

At large electric fields, the Stark effect dominates. Here J and m_J remain good quantum numbers, and for $m_J \neq 0$ the good nuclear spin quantum numbers are $I_{Tl} = 1/2, m_{Tl}$ and $I_F = 1/2, m_F$. For $m_J = 0$, however, spin–spin coupling mixes the nuclear spins into singlet (S=0) and triplet (S=1) states with projection m_S . At low electric fields, the hierarchy reverses: $\mathcal{H}_{\rm rot} \gg \mathcal{H}_{\rm sr}$, $\mathcal{H}_{\rm ss} \gg \mathcal{H}_{\rm S}$. In this regime, the good quantum numbers are J, $F_1 = J + I_{Tl}$, $F = F_1 + I_F$, and m_F .

When molecules traverse from high field to zero field, the $|J,m_J=0,S=1,m_S\rangle$ nuclear-spin triplet states adiabatically evolve into the states $|J,F_1=J+1/2,F=J+1,m_F=m_S\rangle$. The corresponding singlet state $|J,m_J=0,S=0\rangle$ evolves into $|J,F_1=J+1/2,F=J,m_F=0\rangle$. These mappings are essential for interpreting fluorescence detection, which is performed in zero field following state transfer via AP in a region of high field.

II. EXPERIMENTAL OVERVIEW

A schematic of the apparatus is shown in Fig. 2. The cryogenic TlF beam, with mean forward velocity $\bar{v}_f = 184 \, \text{m/s}$, enters the RC chamber, located $\sim 40 \, \text{cm}$ from the source and $\sim 60 \, \text{cm}$ from the cell exit. In this chamber, the molecules interact simultaneously with a

multi-pass laser beam and two focused, free-space, nominally Gaussian-shaped microwave beams that together act to accomplish the RC (see [3] for details).

The molecules then enter the "state preparation A" (SPA) chamber, where the microwave AP takes place. Here, they traverse a region of spatially-varying electric field (E) generated by two energized ring electrodes and surrounding grounded surfaces. This DC field defines the local z axis, and is nominally parallel to the direction of the molecular beam. The spatial profile of the E-field is designed to set the spatial evolution of Stark shifts—and hence the detunings from microwave transitions needed to accomplish AP—for the specific levels of interest. In this DC field, at a location 30.5 cm downstream of the RC region, the molecules encounter a linearly polarized Gaussian beam of microwaves (with polarization parallel to the nominal Efield direction) tuned to resonance with the Stark-shifted $|J=0,m_J=0\rangle \leftrightarrow |J=1,m_J=0\rangle$ (AP1) transition, at a local field strength of 173 V/cm. This is followed 28.6 mm further downstream by a second microwave beam, polarized in the same direction, resonant with the Stark-shifted $|J=1, m_J=0\rangle \leftrightarrow |J=2, m_J=0\rangle$ (AP2) transition at 110 V/cm. Together, these microwave fields drive stepwise population transfer via AP from $|J = 0, m_J = 0\rangle$ to $|J = 1, m_J = 0\rangle$ to $|J = 2, m_J = 0\rangle$ (Fig. 4). The free-space microwave beams are focused at the position of the molecular beam, which they cross at right angles, orthogonally to each other and to the molecular beam.

In the Earth's magnetic field, the nuclear-spin triplet states of $|J=1,m_J=0\rangle$ can mix with the singlet state, leading to unwanted population transfer if the electric field decays too slowly. To mitigate this, an additional grounded plate with a 44.5 mm diameter aperture was installed behind the +450 V electrode, ensuring a rapid field drop after the SPA region and thereby suppressing such mixing.

After SPA, the molecules propagate 36.2 cm down-stream to a region where molecular state populations are detected via laser-induced fluorescence (LIF). A $13\,\mathrm{mm}\,w \times 3\,\mathrm{mm}\,h$ aperture, positioned 25.4 mm upstream of the probe laser, restricts the transverse velocity distribution and spatial spread of the molecular beam. A probe laser orthogonal to the molecular beam then excites selected hyperfine levels, and the resulting fluorescence on the $B\to X$ transition, with a linewidth $\gamma_B=1.6\,\mathrm{MHz}$, is collected by two opposing photomultiplier tubes (PMTs).

A. Electric field generation

The spatially varying electric field is produced by two identical ring electrodes, with 4.5" major and 0.5" minor diameters, plus surrounding grounded sufaces. These electrodes are separated by 6.75" and positioned symmetrically about the SPA chamber center. The first is held

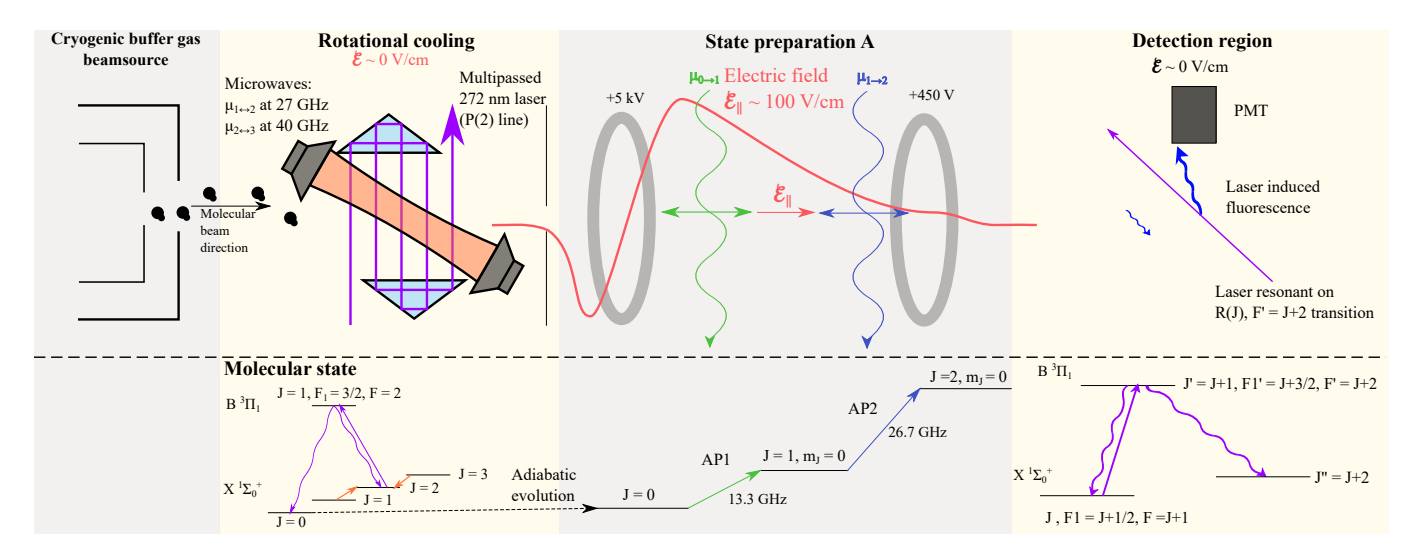


FIG. 2. Schematic of the experimental apparatus. Molecules emerge from the cryogenic buffer-gas beam source and first pass through the rotational cooling region, where optical pumping and microwave transitions transfer population from the J=1,2,3 rotational levels to J=0. The molecules then enter the state preparation region, where they can be transferred to J=1 or J=2 depending on the microwave settings. Finally, the molecules are detected in the detection region by collecting laser-induced fluorescence (LIF) on a PMT. The detection laser can excite different rotational/hyperfine states, allowing determination of their relative populations under different preparation conditions. For convenience in these measurements we operate in the triplet state (S=1), pumping into $|J=0,F=1\rangle$ in RC. Centrex will operate in the singlet state (S=0), pumping into $|J=0,F=0\rangle$ in RC.

at a potential of 5000 V, and the second at 450 V. The resulting field is shaped both to accomplish the desired adiabatic passage transfers, and to suppress unwanted Landau–Zener transitions to other, undesired molecular states. The field strength decreases from $260 \, \text{V/cm}$ to $100 \, \text{V/cm}$ over $10 \, \text{cm}$, corresponding to detuning rates of approximately $20 \, \text{GHz/s}$ for AP1 and $6 \, \text{GHz/s}$ for AP2. The entrance and exit of the SPA chamber are grounded, so the $\mathbf E$ field outside it is nominally zero.

B. Microwave generation and delivery

The $J=0 \rightarrow 1$ transition occurs at 13.34 GHz, and the $J=1 \rightarrow 2$ transition at 26.67 GHz. The 13.34 GHz signal is generated directly by a synthesizer, while the 26.67 GHz signal is obtained by amplifying a 13.33 GHz source and frequency doubling. Both fields are delivered by cylindrically symmetric, spot-focusing lens antennas fed by circular waveguides, producing free-space beams with nearly Gaussian shapes, focused at the molecular beam position. Both microwave beam have $-3\,\mathrm{dB}$ diameters of 2.54 cm at the molecular beam position. The beams enter and exit the chamber through fused silica windows and are terminated in absorbing foam.

Microwave powers of 0.2 mW and 0.05 mW are used for the $J=0 \rightarrow 1$ (Rabi rate $\Omega_{01}\approx 2\pi\times 88\,\mathrm{kHz}$) and $J=1 \rightarrow 2$ (Rabi rate $\Omega_{12}\approx 2\pi\times 35\,\mathrm{kHz}$) transitions, respectively. These correspond to Rabi rates of $\Omega_{01}\approx 2\pi\times 88\,\mathrm{kHz}$ and $\Omega_{12}\approx 2\pi\times 35\,\mathrm{kHz}$, respectively. Simulations indicate that the adiabatic transfer efficiency

is robust against changes in microwave intensity, maintaining high fidelity even for molecules displaced from the beam center. The microwave beam polarizations are aligned along \hat{z} , to selectively drive $\Delta m_J = 0$ transitions. AP1 is centered between the ring electrodes, and AP2 is located 28.6 mm downstream.

We find it important to suppress leakage of the powerful microwaves applied in the RC region, into the SPA chamber where the microwave AP takes place. To accomplish this, an aluminum hexagonal honeycomb mesh with 3/8'' thickness and 1/16'' cell size is installed where molecules exit the RC region and enter the SPA region. The cutoff behavior of the hexagonal cells can be modeled using waveguides of equal cross-sectional area with square or circular geometry, since finite-element analyses show that the fundamental eigenvalue of a regular hexagon differs by < 2% from that of an equal-area square guide [12] and by only $\sim 0.5\%$ from an equalarea circular guide [13]. For the 1/16" hexagonal cells used here, this corresponds to an effective cutoff frequency of $f_{c,11} \approx 106$ GHz for the dominant TE₁₁ mode, well above the RC microwave frequencies. For a 3/8''long cell, transmission at 26.6 GHz is expected to be attenuated by more than 180 dB. A bench test of the honeycomb mesh, however, showed only 60 dB attenuation. Additional suppression of stray microwave fields is provided by mounting Laird Eccosorb HR microwaveabsorbing foam (which reduces reflection by $\geq 20 \text{ dB}$) at the microwave exit windows in the RC region.

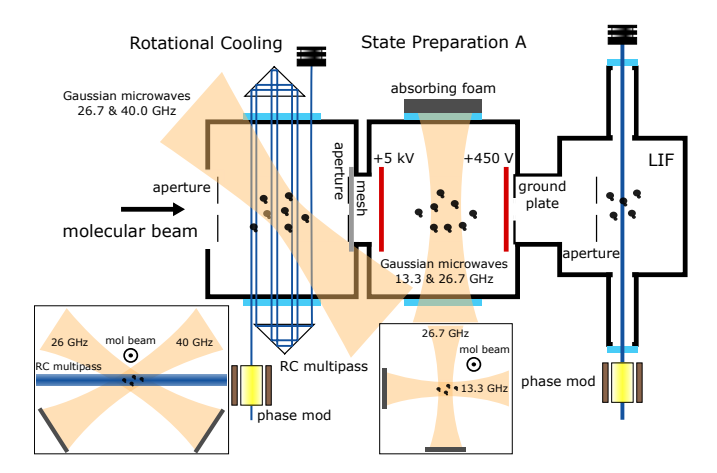


FIG. 3. Schematic overview of the measurement setup. A 271.75 nm laser, phase-modulated on the $P(2) \tilde{F}'_1 = 3/2 F' =$ 2 transition, makes 13 passes through the rotational cooling (RC) region, where it intersects two focused Gaussian microwave beams (inset shows frontal view). An aluminum honeycomb mesh suppresses microwave leakage from RC into SPA. In the SPA chamber, two ring electrodes at +5 kV and +450 V generate a spatially varying electric field, nominally parallel to the molecular beam. The molecular beam then encounters two orthogonal microwave fields that drive successive adiabatic passages. A grounded plate rapidly drives the electric field to zero at the exit of the SPA region. In the detection chamber, an aperture of $13 \,\mathrm{mm}\,w \times 3 \,\mathrm{mm}\,h$ restricts the transverse velocity and beam spread. Populations are measured via laser-induced fluorescence (LIF) from a single 271.75 nm phase-modulated probe beam, collected by two opposing photomultiplier tubes (PMTs) located above and below the plane of the page.

C. Detection Laser

Detection is performed on R-branch transitions, where a line labeled R(J) excites a ground rotational level $|J\rangle$ to an excited level $|J'=J+1\rangle$. We use these transitions to probe population from the J=0,1,2 rotational levels of the $X^1\Sigma_0^+$ ground state. All transitions lie at a wavelength of 271.75 nm and are readily saturated, yielding about two spontaneously emitted photons per molecule before pumping into a dark rotational state [14–16]. The ultraviolet light is generated by frequency quadrupling 1087 nm radiation in two successive stages of second harmonic generation, producing up to 40 mW at 271.75 nm. The probe beam is expanded to elliptical $1/e^2$ diameters of 3.8 mm (width) and 6.2 mm (height), corresponding to a peak intensity of 440 mW/cm². To efficiently cover the transverse Doppler distribution of the molecular beam, the laser is phase-modulated with an electro-optic modulator at frequency γ_B and modulation index $\beta = 3.8$.

D. Measurement scheme for population transfer efficiency

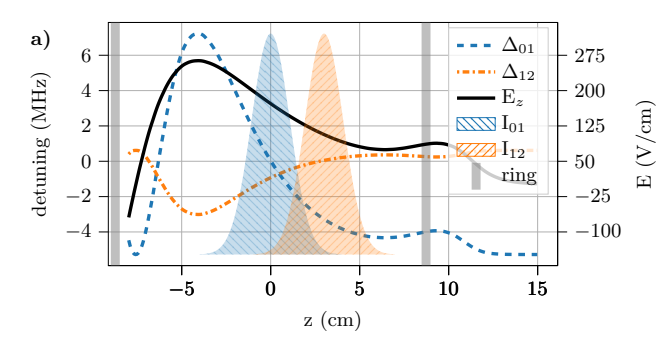
In the $X^1\Sigma_0^+$ ground state, hyperfine splittings are $\sim 100\,\mathrm{kHz}$, much smaller than the natural linewidth of optical transitions to the $B^3\Pi_1$ state, $\gamma_B=1.6\,\mathrm{MHz}$. All ground-state hyperfine levels therefore are typically simultaneously resonant at a single laser frequency. By contrast, hyperfine splittings in the $B^3\Pi_1$ state are typically $\sim 100\,\mathrm{MHz}$ or larger, so the excited-state substructure is fully resolved. This situation couples many ground states with fewer excited states; when the number of ground states exceeds the number of excited states, coherent dark states can form, obscuring the relation between the fluorescence signal and molecular population.

To avoid dark-state formation and provide a clean measure of populations, we probe using only using laser frequencies resonant with the transition to the highest- F' hyperfine level of each excited-state rotational manifold, namely $|\tilde{J}'=J+1,\,F'=J'+1=J+2\rangle$. Selection rules ensure that this laser frequency excites only population in the highest-F hyperfine level of each ground-state rotational manifold, i.e., the level with F=J+1. Here, 2F+1=2J+3 ground state Zeeman sublevels couple to 2F'+1=2J+5 excited state sublevels, eliminating dark states and ensuring that scattering continues until the F=J+1 level is completely pumped into other states.

While convenient for detecting populations after the microwave AP stages, these probe transitions address only the nuclear-spin triplet manifold (S = 1), not the singlet state (S = 0). However, CeNTREX will operate in the S=0 state to provide a well-defined initial state for the Schiff moment measurement. Hence it is important to relate the state transfer efficiency measurements reported here—performed entirely in the S=1manifold—to the efficiencies in the S=0 manifold that are directly relevant to CeNTREXWe find that the transfer efficiencies are independent of S, which makes sense since the microwaves do not couple to the nuclear spins (but only to molecular rotation). Full numerical simulations were performed to confirm that the distinction between S = 0 and S = 1 has no measurable impact on the microwave-driven AP transfer efficiency between rotational states.

To maximize the fluorescence signal during our tests of AP transfer efficiency (using S=1 states), we slightly modify the usual CeNTREX RC protocol [3]. In particular, for the measurements reported here, the optical pumping for RC is performed using the $P(2) \tilde{F}_1' = 3/2 \, F' = 2$ transition, which serves to enhance population in the $|J=0, F=1\rangle$ states. In P-branch notation, a line labeled P(J) connects a ground rotational level J to an excited level J'=J-1. (By contrast, CeNTREX normally employs the $P(2) \, \tilde{F}_1' = 3/2 \, F' = 1$ transition for RC, to enhance the population in the S=0 state $|J=0, F=0\rangle$.)

In the measurements described here, state transfer ef-



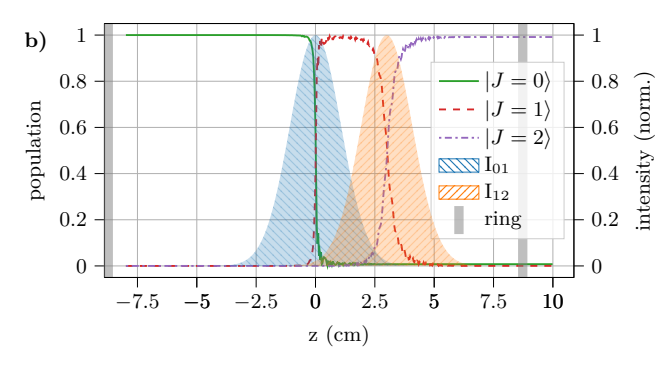


FIG. 4. a) Applied electric field and Stark-shifted detunings of the $|J=0,m_J=0\rangle \leftrightarrow |J=1,m_J=0\rangle$ (blue) and $|J=1,m_J=0\rangle \leftrightarrow |J=2,m_J=0\rangle$ (orange) transitions (Δ_{01} and Δ_{02} , respectively), as functions of the axial position z in the state preparation region. The two microwave frequencies are chosen to be on resonance at the positions corresponding to the maxima of their intensities (I_{01} and I_{12}

, respectively). The nominally Gaussian spatial profiles of the intensity of the two microwave beams are indicated by the shaded curves. The dashed black line shows the z-component of the electric field, E_z . The vertical grey lines indicate the positions of the ring electrodes in the SPA region. b) Simulated populations for molecules initially in $|J=0,m_J=0\rangle$, versus z. Green: $|J=0,m_J=0\rangle$, red: $|J=1,m_J=0\rangle$, purple: $|J=2,m_J=0\rangle$. Two adiabatic passages result in population inversions at the centers of the microwave intensity profiles, where the transitions cross resonance.

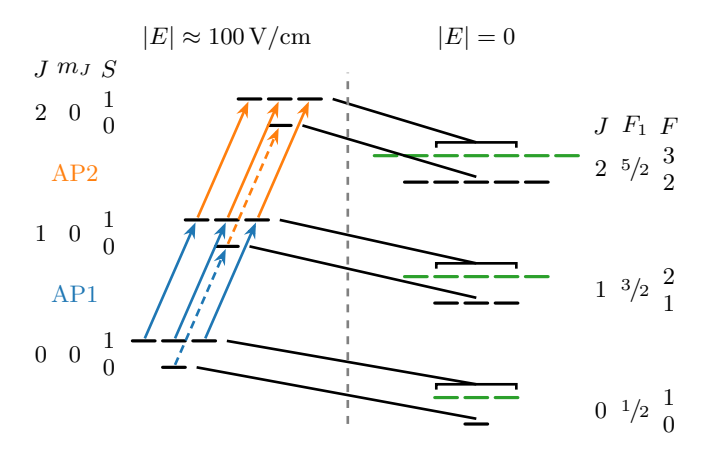


FIG. 5. Adiabatic evolution of $|J,m_J=0,S\rangle$ states from high field ($|E|\approx 100\,\mathrm{V/cm}$) to zero field. Blue arrows indicate the AP1 ($J=0\to 1$) transition, and orange arrows the AP2 ($J=1\to 2$) transition. Nuclear singlet transitions are indicated with dotted lines and nuclear triplet transitions with solid lines. At zero field, the nuclear spin triplet states map to states (in the basis of fully coupled angular momenta) of the form $|J,F_1=J+1/2,F=J+1,m_F=-1,0,1\rangle$, while the singlet state maps to $|J,F_1=J+1/2,F=J,m_F=0\rangle$. Population in the highest F manifold of each J (green) state is detected via LIF.

ficiency is defined as the fraction of molecules transferred from the initially populated states to the target states, with the SPA active. Efficiencies are first optimized for AP1 $(J=0 \rightarrow J=1)$ and subsequently for AP2 $(J=1 \rightarrow J=2)$, keeping AP1 fixed at its optimum.

Since SPA transfers population between $|J, m_J = 0\rangle$ states in fields of order 100 V/cm, it is necessary to track their adiabatic evolution as the field encountered by the molecules evolves to or from E = 0, as is the case just before and after the SPA region. In the absence of magnetic

fields, the triplet states map onto the states (described in the basis of fully-coupled angular momenta) of the form $|J,F_1=J+1/2,F=J+1,m_F=-1,0,+1\rangle$. These states are addressed by the detection laser. The singlet state evolves into $|J,F_1=J+1/2,F=J,m_F=0\rangle$, which is not detected here (Fig. 5).

Finally, states outside the $|J,m_J=0\rangle$ manifold must also be considered. At zero *E*-field these are the $|J,F_1=J+1/2,F=J+1,m_F\neq -1,0,+1\rangle$ states. These states are not affected by the adiabatic passage but contribute background in detection and must be included when extracting efficiencies.

1. Effect of population in unwanted states

If the RC protocol worked perfectly, only states $|J=0\rangle$ would be populated as molecules enter the SPA region. However, in practice, there remains residual population in various sublevels of the $|J=1\rangle$ and $|J=2\rangle$ manifolds. The populations of certain sublevels of these manifolds are not affected by our adiabatic passage protocol, but will appear directly in the LIF signal after the SPA region. In particular, states of the form $|J,F_1=J+1/2,F=J+1,m_F\neq -1,0,+1\rangle$ in zero Efield have this property.

In addition, certain sublevels in these manifolds also can be transferred "backwards" by the AP process itself (i.e., to states with a lower J value but still with F = J+1 so they are detected by LIF). This will result, for example, in nonzero detected LIF signal from the states meant to be depopulated by the AP process.

Both these effects complicate the analysis needed to correctly translate the measured LIF signals into true state transfer efficiencies. Next we discuss the procedure we use to account for these effects.

2. AP1 transfer efficiency

We denote the efficiency of transfer in AP1 as ϵ_{01} . To determine its value, we measure LIF signalsproportional to the populations in zero E-field after the SPA region—from the $|J=0,F=1\rangle$ and $|J=1,F=2\rangle$ states, both with and without the AP1 microwaves applied. We denote these raw signals (with the obvious correspondences) as $S_{0/1}^{\rm ON/OFF}$. The $S_0^{\rm OFF}$ and $S_1^{\rm OFF}$ signals are simply proportional to the overall photon detection efficiency K, the total number of Zeeman sublevels 2F+1=2J+3, the population n_J of each Zeeman sublevel at the input to the relevant AP region (assumed to all be the same within the $|J, F = J + 1\rangle$ manifold), and the average number of LIF photons emitted when probing each of these manifolds, n_{γ_I} . Specifically, we write

$$S_0^{\text{OFF}} = 3n_{\gamma_0} n_0 K, \tag{5a}$$

$$S_1^{\text{OFF}} = 5n_{\gamma_1} n_1 K. \tag{5b}$$

We expect $n_1 \ll n_0$ after rotational cooling.

When the AP1 microwaves are applied, we detect the analogous signals, $S_{0,1}^{ON}$. The expected size of these signals must account for both the desired transfer $J=0 \rightarrow$ J=1 and the undesired backward transfer $J=1 \rightarrow$ J=0 (arising from unwanted initial population in the $|J=1, F=2\rangle$ manifold), both occurring with efficiency ϵ_{01} . This leads to the expressions

$$S_0^{\text{ON}} = 3n_{\gamma_0} [(1 - \epsilon_{01})n_0 + \epsilon_{01}n_1]K,$$
 (6a)

$$S_1^{\text{ON}} = n_{\gamma_1} [5n_1 + 3\epsilon_{01}(n_0 - n_1)]K,$$
 (6b)

In Eq. (6a), the first term comes from incomplete transfer of $|J=0\rangle$ population into $|J=1\rangle$, and the second term from backward transfer from residual $|J=1\rangle$ population. In Eq. (6b), the first term comes from the residual population in $|J=1\rangle$, and the second term accounts both for successful transfer from $|J=0\rangle$ and backwards transfer from residual $|J=1\rangle$ population.

To eliminate the poorly known quantities K and n_{J} , it is convenient to define ratios of the signals as follows:

$$R_0 = S_0^{\text{ON}} / S_0^{\text{OFF}},$$
 (7a)

$$R_0 = S_0^{\text{ON}} / S_0^{\text{OFF}},$$
 (7a)
 $R_{10}^{\text{OFF}} = S_1^{\text{OFF}} / S_0^{\text{OFF}},$ (7b)

$$R_{\rm t} = S_1^{\rm ON} / S_0^{\rm OFF}.$$
 (7c)

Note that for high efficiency and low unwanted popula-

tions, we expect R_0 , $R_{10}^{\rm OFF} \ll 1$, and $R_{\rm t} \sim n_{\gamma_1}/n_{\gamma_0}$. The values of n_{γ_J} can be calculated from known branching ratios [14–16] for decay of the $|J'=J+1,F'=J'+1\rangle$ states excited by the laser into different hyperfine/rotational levels of the ground state (in the approximation that the probe transitions are fully saturated, which we find is well satisfied). We find $n_{\gamma_0} = 1.92$, $n_{\gamma_1} = 2.10$, and $n_{\gamma_2} = 2.13$.

With the measured ratios of signals, there are two distinct ways to determine the efficiency ϵ_{01} from our

data. One uses R_0 , which nominally corresponds to the fractional removal of $|J=0,F=1\rangle$ population by the AP1 microwaves; the other uses R_t , which nominally corresponds to the fraction of the original population in $|J=0\rangle$ that is transferred into $|J=1\rangle$. We hence define two different "apparent" efficiencies, derived from these different ratios and corresponding to removal of population from $|J=0\rangle$ $(\epsilon_{01}^{\mathrm{rem}})$, or appearance of population in $|J=1\rangle$ $(\epsilon_{01}^{\text{app}})$. These are related to the signal ratios via the relationships

$$\epsilon_{01}^{\text{rem}} = (1 - R_0) / \left(1 - \frac{3n_{\gamma_0}}{5n_{\gamma_1}} R_{10}^{\text{OFF}} \right),$$
(8a)

$$\epsilon_{01}^{\text{app}} = \frac{n_{\gamma_0}}{n_{\gamma_1}} \left(R_{\text{t}} - R_{10}^{\text{OFF}} \right) / \left(1 - \frac{3n_{\gamma_0}}{5n_{\gamma_1}} R_{10}^{\text{OFF}} \right).$$
(8b)

Both methods should give consistent values of ϵ_{01} if all population removed from $|J=0, F=1\rangle$ is ultimately transferred into $|J=1, F=2\rangle$ states. Writing these relationships in terms of the ratios makes it evident that in the limit where $R_{10}^{\rm OFF} \to 0$, $R_0 \to 0$ and and $R_t \to n_{\gamma_1}/n_{\gamma_0}$, $\epsilon_{01}^{\rm rem} = \epsilon_{01}^{\rm app} = 1$.

3. AP2 transfer efficiency

Extracting the AP2 transfer efficiency requires probing the populations in $|J=1, F=2\rangle$ and $|J=2, F=3\rangle$. We probe $|J=1, F=2\rangle$ as for AP1. For $|J=2, F=3\rangle$, we tune the probe laser to excite the $|\tilde{J}'=3, F'=4\rangle$ state using the $R(2) \tilde{F}'_1 = 7/2 F' = 4$ transition.

Including residual J=2 population after the RC region and finite AP1 efficiency, the measured signals Σ (defined in analogy with the signals for AP1) are given

$$\Sigma_1^{\text{OFF}} = S_1^{\text{ON}} = n_{\gamma_1} \left[5n_1 + 3\epsilon_{01}(n_0 - n_1) \right] K$$
 (9a)

$$\Sigma_1^{\text{ON}} = n_{\gamma_1} \left(3\epsilon_{12} n_2 + 2n_1 \right)$$
 (9b)

$$+3n_{\gamma_1} \left[1 - \epsilon_{12} \left(\epsilon_{01} n_0 + n_1 (1 - \epsilon_{01})\right)\right] K$$
 (9c)

$$\Sigma_2^{\text{OFF}} = 7n_{\gamma_2} n_2 K \tag{9d}$$

$$\Sigma_2^{\text{ON}} = n_{\gamma_2} \left[4n_2 + 3\epsilon_{12} \left(\epsilon_{01} n_0 + n_1 (1 - \epsilon_{01}) \right) \right]$$
 (9e)

$$+3n_{\gamma_2}n_2(1-\epsilon_{12})K,$$
 (9f)

where ϵ_{12} is the $|J=1\rangle \rightarrow |J=2\rangle$ transfer efficiency due to the AP2 microwaves. Note that here, "ON/OFF" corresponds to the AP2 microwaves; for all these measurements, AP1 is operated at maximum transfer efficiency.

For simplicity, we combine these signal relations with only the expression for $\epsilon_{01}^{\text{app}}$ [Eq. (8b)] to find the following expressions for the apparent AP2 transfer efficiencies:

$$\epsilon_{12}^{\text{rem}} = \frac{35 \, n_{\gamma_2} \left(\Sigma_1^{\text{OFF}} - \Sigma_1^{\text{ON}} \right)}{d}, \tag{10a}$$

$$\epsilon_{12}^{\text{app}} = \frac{35 \, n_{\gamma_1} \left(\Sigma_2^{\text{ON}} - \Sigma_2^{\text{OFF}} \right)}{d},\tag{10b}$$

where the common divisor is

$$d = 35 S_1^{\text{ON}} n_{\gamma_2} - 14 S_1^{\text{OFF}} n_{\gamma_2} - 15 n_{\gamma_1} \Sigma_2^{\text{OFF}}.$$
 (11)

Note that we have not found a form of these equations that makes their limiting forms easily apparent, so we leave them in terms of the raw signals.

4. Total SPA transfer efficiency

The total $|J=0\rangle \rightarrow |J=2\rangle$ transfer efficiency in the SPA region, ϵ_{02} , is given by by the product of the AP1 and AP2 efficiencies: $\epsilon_{02} = \epsilon_{01}\epsilon_{12}$. The apparent value(s) of this quantity can be related to the various signals using the expressions above.

III. RESULTS

A. AP1 transfer efficiency

To experimentally determine the AP1 transfer efficiency, we initially set the RC region parameters to their usual optimized settings (i.e., both RC microwaves and the RC laser on resonance), to maximize the population detected in the $|J=0,F=1\rangle$ states. Next we determine the optimal AP1 microwave power, i.e., the power that minimizes the observed value of R_0 , and the optimal AP1 microwave frequency, i.e., the frequency that maximizes the observed value of R_t . We found, as expected, that the measured values of R_0 and R_t were only weakly sensitive to both the power and frequency of the AP1 microwaves, over a fairly broad range around their expected optimum values. In practice, suitable performance is obtained for powers between 0.1 mW and 0.6 mW; the current setpoint is 0.2 mW. Similarly, varying the microwave frequency by up to $\pm 1\,\mathrm{MHz}$ around the resonance of 13.34 GHz does not measurably change the observed performance. The central frequency agrees with the expected value from the rotational splittings and the Stark shift.

In this configuration, we expected to find $\epsilon_{01} \approx 1$ —and indeed, the measured apparent removal efficiency was $\epsilon_{01}^{\rm rem} = 0.97(1)$. However, the measured apparent appearance efficiency was much lower: $\epsilon_{01}^{\rm app} = 0.23(2)$.

We traced the origin of this discrepancy to leakage of the very high power microwaves from the RC region (with typical peak power of 0.5 W) into the SPA chamber, where the typical peak AP1 microwave power is only 0.05 mW. Specifically, the discrepancy between apparent removal and appearance efficiencies was found to arise from population transfer from $|J=1\rangle$ to $|J=2\rangle$ in the SPA region, induced by microwaves resonant with the $J=1 \rightarrow J=2$ transition at zero E-field that leak from the RC region into the SPA region. Note that molecules are also near resonance with this frequency at various positions in the SPA region where the E-field is small

(see Fig. 7). These stray microwaves reduce the measured population of $|J=1\rangle$ after the SPA region, but do not affect the population of $|J=0\rangle$ states. Hence, the apparent efficiency determined from removal of the $|J=0\rangle$ state can still provide sensible results, while the apparent efficiency determined from appearance into the $|J=1\rangle$ state will be smaller than the actual efficiency. Because the microwave power in the RC region is about 10^4 times larger than that in the SPA region, even a very small fractional leakage produces measurable effects in the SPA region.

This interpretation was initially confirmed by measurements with the $J=1\leftrightarrow 2$ microwaves in the RC region switched off. Further confirmation—and a solution to this problem—was found by deliberately tuning the $J=1\to 2$ microwave frequency in the RC region around the zero-field resonance. Detuning these microwaves slightly off resonance did not affect the RC efficiency. However, it dramatically improved the AP1 apparent efficiency of appearance (Fig. 6a).

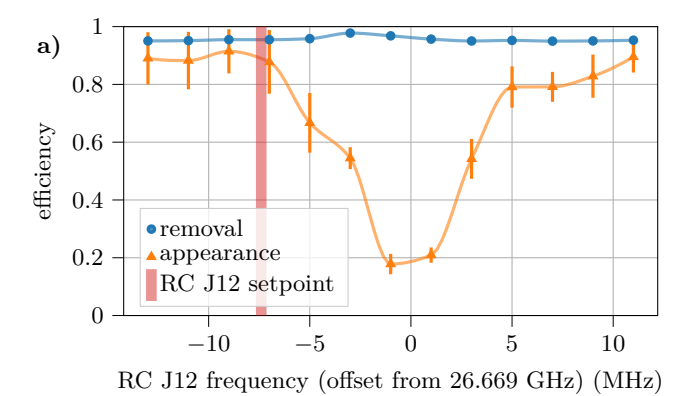
We found that when the RC $J=1\leftrightarrow 2$ microwaves were detuned 7.4 MHz below the nominal $J=1\leftrightarrow J=2$ transition frequency (26.669 GHz), the apparent appearance efficiency reached its maximum value, while the apparent removal efficiency was unchanged. Under these conditions, apparent removal and appearance efficiencies of $\epsilon_{01}^{\rm rem}=0.95(1)$ and $\epsilon_{01}^{\rm app}=0.88(11)$ were achieved for AP1. Since these apparent AP1 transfer efficiencies are consistent with each other, we assign the actual AP1 transfer efficiency as the (unweighted) average of the two apparent values: $\epsilon_{01}=0.92(6)$.

B. AP2 transfer efficiency

The AP2 transfer efficiency as a function of the detuning of the AP2 $J=1\to 2$ microwave from the expected peak value is shown in Fig. 6b. This frequency scan is performed after optimizing the AP2 microwave power at the frequency of peak efficiency. With the AP2 microwave detuning set for maximal AP2 efficiency, the peak values of the apparent removal and appearance efficiencies are $\epsilon_{12}^{\rm rem}=0.99(1)$ and $\epsilon_{12}^{\rm app}=1.11(10)$, respectively. As before, we combine these to assign the actual AP2 transfer efficiency: $\epsilon_{12}=1.05(5)$. Maximal AP2 efficiency is achieved at 26.6684 GHz, which is offset by $-0.38\,\rm MHz$ from the value expected from the rotational splittings and the Stark shift.

Unlike the case for AP1, the presence of the microwave field driving the $J=2\leftrightarrow 3$ transition in the RC region had no measurable effect on the AP2 efficiency. However, the frequency scan in Fig. 6b shows some unanticipated features in the apparent efficiency of appearance (rather than a simple peak). We have qualitatively understood these features, and explain them next.

The reason for the unexpectedly low apparent efficiency of appearance on the low-frequency side of the peak in Fig. 6b can be understood from Fig. 7. In par-



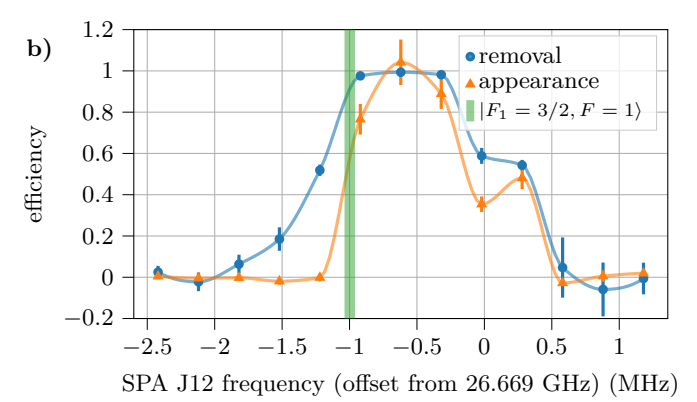


FIG. 6. Apparent transfer efficiencies based on removal and appearance measurements of the AP1 $J=0 \to 1$ and AP2 $J=1 \to 2$ microwave transitions. In both panels, error bars indicate the 95% confidence level, and the connecting lines serve only as visual guides. The 26.669 GHz offset corresponds to the RC J12 microwave resonance. a) Apparent efficiencies for the AP1 $J=0 \to 1$ transfer, versus the detuning from resonance of the high-power $J=1 \to 2$ microwaves in the RC region. This clearly shows improved apparent efficiency in appearance when the RC J12 microwaves are detuned from resonance. With the RC microwaves on resonance, the apparent removal and appearance efficiencies are very different: 0.97(1) and 0.23(2), respectively. When the RC J12 microwaves are detuned by -7.4 MHz, the apparent transfer efficiencies are instead consistent with each other (as expected): $\epsilon_{01}^{\rm rem}=0.95(1)$ and $\epsilon_{01}^{\rm app}=0.88(11)$. The efficiency of RC was not noticeably changed with this detuning applied. We thus set the RC J12 microwave detuning at -7.4 MHz for subsequent characterization of AP2 efficiencies. b) Apparent efficiencies for AP2 $J=1 \to 2$ transfer, versus detuning of the J12 microwaves in the SPA region. with maximal removal and appearance efficiencies of $\epsilon_{12}^{\rm rem}=0.99(1)$ and $\epsilon_{12}^{\rm app}=1.11(10)$, respectively. The vertical green line marks the resonance frequency of the transfer to $|F1=3/2, F=1\rangle$, rather than the intended $|F1=5/2, F=3\rangle$, consistent with Fig. 7.

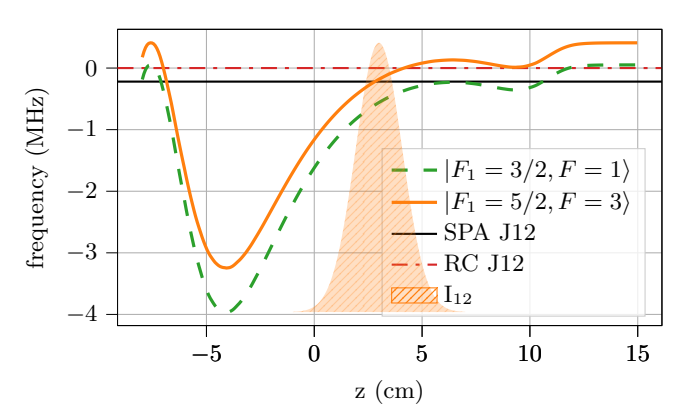


FIG. 7. Detuning of the $|J=1,F_1=3/2,F=2,m_F=0\rangle \rightarrow J=2$ transition driven by linearly polarized microwaves, offset by 26.669 GHz; the RC J12 microwave resonance. The target state is $|F_1=5/2,F=3\rangle$. The solid horizontal line marks the AP2 frequency, and the dash-dotted line the RC $J=1\rightarrow 2$ frequency. The shaded curve shows the assumed microwave intensity profile. State labels are given in the coupled basis at zero field.

ticular: when the frequency of the microwaves driving the $J=1\to 2$ transition in AP2 is shifted downward, the undesired state $|J=2,F_1=3/2,F=1\rangle$ state is Starkshifted into resonance at a position near (or just before) the position of the AP2 microwave beam's peak intensity. When this occurs, the AP2 microwaves can transfer population to this undesired level, which is not addressed by the detection laser. Hence, this effect reduces the apparent efficiency of appearance.

The diminished apparent efficiency of appearance over a small frequency range on the high-frequency side of the peak in Fig. 7b is also understood. This feature originates from a spatially diffuse microwave background field that arises from scattering of the (nominally Gaussian-distributed) AP2 microwave field. This background field can drive population transfer from $|J=1\rangle$ into the same undesired state, and it comes into resonance with this Stark-shifted state at positions near 11 cm in Fig. 7.

C. Total SPA transfer efficiency

Combining the measured efficiencies from both AP1 and AP2 stages yields a total apparent efficiency (for appearance) of 0.97(8) for the transfer $J=0 \rightarrow 2$ in the SPA region.

IV. SUMMARY AND OUTLOOK

We have demonstrated microwave-driven adiabatic passage in a spatially varying electric field with a beam of cryogenic TlF molecules. Rotational state transfer efficiencies of $\epsilon_{01}=0.88(11)$ for AP1 and $\epsilon_{12}=1.11(10)$ for AP2 were achieved, corresponding to a total transfer efficiency from $|J=0\rangle$ to $|J=2\rangle$ of $\epsilon_{02}=0.97(8)$ for population transfer from $J=0 \rightarrow J=2$.

Since CeNTREX will operate in the S=0 state rather than the S=1 states studied here, we again note that the transition properties remain essentially unchanged

between these two cases. For example, the transition frequencies for the S=1 vs. S=0 cases shift by only $3\,\mathrm{kHz}$ for AP1 and $38\,\mathrm{kHz}$ for AP2, far smaller than the $\gtrsim 700$ kHz range of microwave frequencies over which the state transfer efficiency ϵ_{02} remains consistent with 1. The corresponding differences in Rabi rates are $< 2\pi \times 1\,\mathrm{kHz}$ for AP1 and $\approx 2\pi \times 1\,\mathrm{kHz}$ for AP2. These changes are small compared to the current Rabi rates, and the dependence on the Rabi rates is very weak around the optimum values. Hence, we expect no noticeable change in the overall SPA state transfer efficiency when we switch to operation in the S=0 state.

Centrex requires two additional state-preparation regions: one to prepare the state where the Schiff moment measurement will be performed, and another to convert the final nuclear spin state into populations of different rotational states, for readout of the spin [1]. The robust and high-fidelity transfer of population into

specific hyperfine states of TlF molecules that we have demonstrated here can also be applied to these other state-preparation regions in CeNTREX. Altogether, the anticipated high efficiencies for all quantum-coherent state preparation regions will be sufficient for reaching the targeted sensitivity to the ²⁰⁵Tl Schiff moment in CeNTREX[1].

ACKNOWLEDGMENTS

We are grateful for support from the John Templeton Foundation; the Heising-Simons Foundation; a NIST Precision Measurement Grant; NSF-MRI Grants No. PHY-1827906, No. PHY-1827964, and No. PHY-1828097; NSF Grant No. PHY-2110420; and the Department of Energy (DOE), Office of Science, Office of Nuclear Physics, under Contract No. DEAC02-06CH11357 and Grant No. DE-SC0024667.

- O. Grasdijk, O. Timgren, J. Kastelic, T. Wright, S. Lamoreaux, D. DeMille, K. Wenz, M. Aitken, T. Zelevinsky, T. Winick, and D. Kawall, Centrex: a new search for time-reversal symmetry violation in the ²⁰⁵Tl nucleus, Quantum Science and Technology 6, 044007 (2021).
- [2] P. Sandars, Measurability of the proton electric dipole moment, Physical Review Letters 19, 1396 (1967).
- [3] O. Grasdijk, D. DeMille, J. Kastelic, S. Lamoreaux, O. Timgren, K. Wenz, T. Zelevinsky, and D. Kawall (Centrex Collaboration), Rotational-hyperfine cooling of ²⁰⁵TlF in a cryogenic beam, Phys. Rev. A 112, 022803 (2025).
- [4] E. A. Hinds and P. G. Sandars, Experiment to search for P- and T-violating interactions in the hyperfine structure of thallium fluoride, Physical Review A 21, 480 (1980).
- [5] E. B. Treacy, Adiabatic inversion with light pulses, Physics Letters A 27, 421 (1968).
- [6] B. W. Shore, M. V. Gromovyy, L. P. Yatsenko, and V. I. Romanenko, Simple mechanical analogs of rapid adiabatic passage in atomic physics, American Journal of Physics 77, 1183 (2009), https://doi.org/10.1119/1.3231688.
- [7] M. M. T. Loy, Observation of Population Inversion by Optical Adiabatic Rapid Passage, Physical Review Letters 32, 814 (1974), publisher: American Physical Society.
- [8] D. Budker, D. F. Kimball, and D. P. Demille, Atomic Physics: An Exploration Through Problems And Solutions (Oxford University Press, 2008).
- [9] C. Wittig, The Landau-Zener Formula, The Journal

- of Physical Chemistry B **109**, 8428 (2005), publisher: American Chemical Society.
- [10] N. R. Hutzler, H.-I. Lu, and J. M. Doyle, The buffer gas beam: An intense, cold, and slow source for atoms and molecules, Chemical reviews 112, 4803 (2012).
- [11] N. R. Hutzler, M. F. Parsons, Y. V. Gurevich, P. W. Hess, E. Petrik, B. Spaun, A. C. Vutha, D. DeMille, G. Gabrielse, and J. M. Doyle, A cryogenic beam of refractory, chemically reactive molecules with expansion cooling, Phys. Chem. Chem. Phys. 13, 18976 (2011).
- [12] A. Vaish and H. Parthasarathy, Frequencies of propagation of electromagnetic waves in a hexagonal waveguide, International Journal of Microwave and Optical Technology 5, 305 (2010), manuscript ID: IJMOT-2010-6-592.
- [13] K. Zdeněk and S. Jiří, Numerical computation of cutoff frequency of irregular hexagonal waveguide, in 2012 International Conference on Applied Electronics (2012) pp. 163–166.
- [14] E. B. Norrgard, E. R. Edwards, D. J. McCarron, M. H. Steinecker, D. DeMille, S. S. Alam, S. K. Peck, N. S. Wadia, and L. R. Hunter, Hyperfine structure of the $B^3\Pi_1$ state and predictions of optical cycling behavior in the $X \to B$ transition of TlF, Phys. Rev. A **95**, 062506 (2017).
- [15] G. Meijer and B. G. Sartakov, Λ doubling in the $B^3\Pi_1$ state of tlf, Phys. Rev. A **101**, 042506 (2020).
- [16] O. Timgren, Progress towards a measurement of timereversal symmetry violation in thallium fluoride, Ph.D. thesis, Yale Graduate School of Arts and Sciences (2023).